RSC Advances

ROYAL SOCIETY OF CHEMISTRY

www.rsc.org/advances

Control of Manganese Dioxide Crystallographic Structure in the Redox Reaction between Graphene and Permanganate Ions and Their Electrochemical Performance

Chenchen Ji [1], Haoqi Ren[3], Shengchun Yang[1,2]*

1 School of Science, Key Laboratory of Shanxi for Advanced Materials and Mesoscopic Physics, State Key Laboratory for Mechanical Behavior of Materials, Xi'an Jiaotong University, Xi'an, 710049, People's Republic of China.

2 Collaborative Innovation Center of Suzhou Nano Science and Technology, Suzhou Academy of Xi'an jiaotong University, 215000, Suzhou, People's Republic of China.

3 Department of Chemistry, Fudan University, Shanghai 200433, People's Republic of China.

***Corresponding author**

Tel: +86-29-82663034. Fax: +86-29-82665995. E-mail: ysch1209@mail.xjtu.edu.cn (S.C. Yang).

ABSTRACT:

MnO_2 with α+γ-, δ-, and α-phases were synthesized by using graphene as sacrificial template in a proposed $KMnO_4$-graphene-H_2SO_4 reaction system. The as-prepared products were characterized with X-ray diffraction technique, Raman spectroscopy, and transmission electron microscopy. The structural analysis reveals that the cation concentration, i.e. H^+ and K^+, has a profound effect on both the crystallographic structures and morphologies of the final products. The relatively higher K^+ concentration but lower H^+ concentration facilitates the formation of *δ*-phased MnO_2 with a petal-like structure, and the lower concentration of both K^+ and H^+ cations is more conducive to the formation of a mixed phase of (α+γ) MnO_2. Further increase of the concentration of H^+, forming the *α*-phased MnO_2 nanorods is preferred. The electrochemical properties for supercapacitors indicate that the electrochemical performances of MnO_2 strongly depend on their crystallographic structures, and they present a Faradaic reactivity sequence of *δ*- > *α*- > *α*+*γ*-MnO_2.

Keywords: MnO_2; Graphene; template; Various crystallographic structures; Supercapacitor performance

1. INTRODUCTION

The limited availability of fossil fuels coupled with the growing demand for sustainable and renewable development has led to a significant attention in developing regenerative energy conversion/storage devices.[1-7] As one of the most effective and practical technologies for energy storage components, supercapacitors (SC) have attracted much attention due to their high power density, excellent

reversibility and long cycle-life. SC can be classified into electrical double-layer capacitance (EDLC) and Faradic pseudocapacitance depended on the charge storage mechanism.[3,6,8] Compared with the former one, Faradic pseudocapacitance can provide more specific capacitance than the EDLC of carbon-based electrode materials,[9] due to a fast and reversible Faradic redox reaction.[3] Hence, great efforts have been focused on searching for pseudocapacitance materials with improved electrochemical performance.[8]

Among the various Faradic pseudocapacitance electrode materials, MnO_2 posesses many significant advantages, such as the high theoretical pseudo-capacitance (~1400 F/g)[9], wide voltage windows, low-cost and environmental compatibilities.[1,5,6,8,10,11] However, MnO_2 obtained by traditional method always possesses a low specific surface area,[12] leading to a poor performance in their applications in SC.[13] Therefore, searching for special synthesis method of MnO_2 materials with a significantly increased specific surface area is urgently needed.

Graphene, the thinnest two-dimensional carbon structure, has shown exceptional physicochemical properties that has been making a tremendous impact in the areas of physics, chemistry and materials science. [14-19] Its unique structure suggests it may have great potential for providing new approaches and critical improvements in the material synthesis. For example, the sacrificial template method by means of *in situ* replacement with the framework of graphene to yield the corresponding materials can dramatically increase the specific surface area and performance of the prepared materials. Typically, several approaches have been developed for the fabrication of

MnO_2 pseudocapacitance materials by using graphene as the sacrificial template. Chen *et al.*[20] reported a method by *in situ* replacing the framework of graphene with MnO_2 in which the layered structure of graphene was transmitted to the as-prepared metal oxides. Such lamella-like structure bestowed the as-prepared MnO_2 sample an excellent electrochemical stability as the supercapacitor electrode. Zhao *et al.*[13] synthesized the MnO_2 nanosheets with graphene oxide as a sacrificial template. The morphology transmission from graphene oxide to δ-type MnO_2 nanosheets results in an especially high surface area (157 m^2/g) and a high performance in Faraday pseudocapacitances.

Although the single-phased MnO_2 nanomaterials with controllable morphology synthesized by graphene template method have been reported by several groups, as mentioned above,[10,13,20] it is still hard to control their crystal structure by using such method. In fact, besides the morphologies, the electrochemical properties of MnO_2 are also largely depended on its crystallographic structure.[21,22] In current work, three types of MnO_2 (α+γ-, δ-, and α-phases) with high specific surface area were synthesized using graphene as a sacrificial template in a $KMnO_4$-graphene-H_2SO_4 reaction system. The control of crystal phase and morphology was realized by simply varying the cation type and cation concentration (K^+, H^+) in the reaction system. To our knowledge, it is for the first time to obtain the different crystallographic structures of MnO_2 by using graphene as a sacrificial template. The further studies on the crystallographic structure-dependent electrochemical reactions and energy storage behaviors of the obtained MnO_2 electrode materials show that the δ-MnO_2 electrode

presents the highest specific capacitance than that of the α-MnO_2 and α+γ-MnO_2.

2. EXPERIMENTAL SECTION

2.1. Material Synthesis. Graphene was purchased from the Institute of Shanxi Coal Chemistry, Chinese Academy of Sciences. All chemical reagents in this work were analytical grade and used as received. Three kinds of MnO_2 with different crystalline structures were prepared by using graphene as the sacrificial template.

Synthesis of α+γ-Phased MnO_2. The MnO_2 samples were prepared as Chen's method after a minor modification.[23] In a typical procedure, graphene (10 mg) was ground with $KMnO_4$ (100 mg) by using an agate mortar and pestle to get a powder mixture. 10 mL deionized (DI) water was then added and stirred at room temperature (16 °C) for 20 min. Then, 50 μL concentrated H_2SO_4 (95–98 wt.%) was added to the system and stirred at room temperature for additional 1 h. The solution was then heated in an oil bath at 85 ℃ for 1 h. After that, the reaction mixture was removed from the heat source, and cooled down to room temperature. The precipitates were collected by centrifugation for several times and then the product was dried at 65 ℃ for 12 h.

Synthesis of δ-Phased MnO_2 Nanosheets. The *δ*-phased MnO_2 nanosheets were prepared under the same conditions for the *α+γ*-phased MnO_2 nanorod, except that the amount of $KMnO_4$ was increased to 150 mg.

Synthesis of α-Phased MnO_2 Nanorods. The *α*-phased MnO_2 nanorods were prepared under the same conditions with the *α+γ*-phased MnO_2 sample, except that the volume of H_2SO_4 was 100 μL. In addition, to explore the formation mechanism of

MnO_2 with different crystalline structures, the influence of H_2SO_4 and $KMnO_4$ concentration were also investigated.

2.2. Material characterization. The crystal structure of the samples was characterized by powder X-ray diffraction (XRD, Bruker D8 Advance X-ray diffractometer) with a Cu Kα X-ray source (λ=1.5405 Å) in the range between 15 and 80°. The morphology and microstructure were examined by scanning electron microscopy (SEM, JEOL JSM-7000F) and transmission electron microscopy (TEM, JEOL JEM-3010). Nitrogen adsorption/desorption was carried out at 77.3 K by means of an ASAP 2020M Xtended Pressure Sorption Analyzer. The Raman spectrum was recorded on the HORIBA JOBIN YVON Raman spectrometer using laser excitation at 514 nm from an argon ion laser source. Thermogravimetric analysis (TGA) curves were measured by using a Q1000DSC+LNCS+FACS Q600SDT thermoanalyzer systems from room temperature to 800 °C in an air atmosphere. The electronic structure of the prepared samples was analyzed by X-ray photoelectron spectroscopy (XPS, AXIS ULTRA, Kratos Analytical Ltd.) analysis.

2.3. Electrochemical Measurement. The electrodes of the electrochemical capacitors were fabricated by mixing the prepared powder with 10 wt% acetylene black and 5 wt % polytetrafluorene-ethylene (PTFE) binder of the total electrode mass. A small amount of alcohol was added to the mixture, forming the homogeneous paste. The mixture was pressed onto the nickel foam current collectors (3.0×1.0 cm^2) to make the electrodes. Every electrode contains the active material approximately 5.0 mg/cm^2. Electrochemical characterization was carried out in a conventional

three-electrode cell in 1 M Na_2SO_4 electrolytes. Platinum foil and Ag/AgCl electrode were used as the counter and reference electrode, respectively. Cyclic voltammetry (CV) and galvanostatic charge/discharge measurements were conducted using a CHI 660e electrochemical workstation (Shanghai Chenhua Co. Ltd., China). Long-term galvanostatic charge/discharge cycling tests were performed on a multi-channel battery analyzer (Land, CT2001A).

3. RESULTS AND DISCUSSION

The graphene features a transparent layered structure and a high surface area of 625.2 m^2/g as proven by SEM, TEM and nitrogen sorption measurements (Fig. 4a for BET measurement and Fig. S1 in Supporting Information, SF, for SEM and TEM images), respectively. Due to the thin-layered structure, almost all the carbon atoms in the graphene are reactive, thus it can be oxided by MnO_4^- ions in an acid solution through the following chemical reaction equation (1): [23]

$$4KMnO_4 + 3C + 2H_2SO_4 \rightarrow 4MnO_2 + 3CO_2 + 2K_2SO_4 + 2H_2O \quad (1)$$

The phase structure of the prepared samples was characterized by the XRD analysis and shown in Fig. 1. The pristine graphene only shows a weak and broad peak in the range of 20-28° (Fig. 1a). The XRD pattern in Fig. 1b can be assigned to the tetragonal phase of α-type MnO_2 (JCPDS 44-0141).[24] The α-MnO_2 consists of interlinking double chains of edge-sharing basic units octahedral [MnO_6], which are linked at corners to form (2 × 2) and (1 × 1) tunnels (Fig. 1), and the size of (2 × 2) and (1 × 1) tunnels is 4.6 × 4.6 and 2.3 × 2.3 Å, respectively.[1] The broad peaks at 2θ = 37.1, and 65.5° in Fig. 1c can be indexed to the poorly crystalline phased δ-type MnO_2

(JCPDS 18-0802)[22]. The δ-phased MnO_2 is a 2D layered structure with an interlayer separation of ~ 7 Å between the MnO_6 octahedra, in which a large amount of stabilizing cations, such as K^+ was considered to fill those space.[22] Unlike the above patterns, the diffraction pattern in Fig. 1d, consists of the peaks resulting from both the α- and γ-phased MnO_2 (JCPDS 14-0644),[22,25,26] suggesting that the sample possesses a mixed phase. In all cases, the broad peak of graphene located in the range of 20-28° disappeared, indicating that the framework of the graphene was replaced by MnO_2.

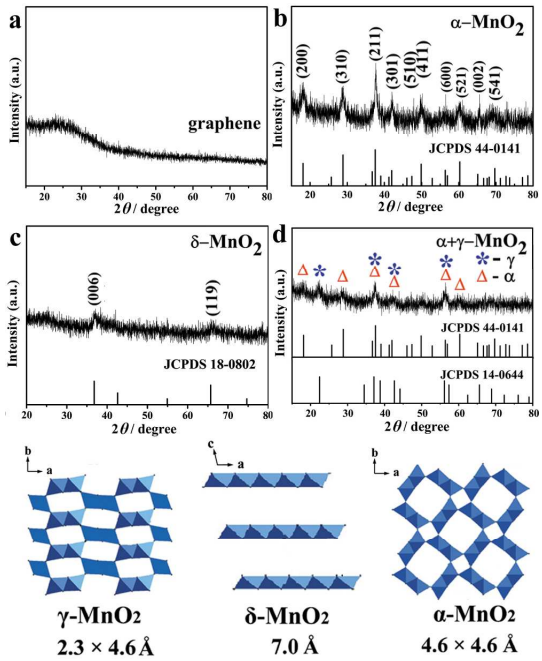

Fig.1. XRD patterns of the (a) graphene, (b) α-MnO_2, (c) δ-MnO_2 and (d) α+γ-MnO_2 sample, and the corresponding schematic illustration of MnO_2 crystal structures.

The morphology and microstructure of the synthesized MnO_2 samples were characterized by SEM and TEM, as shown in Fig. 2. The SEM and TEM observations clearly indicate that both the nanorod- and plate-like structures present in the mixed

phase of α+γ-MnO_2 sample (Fig. 2a and 2d). The high-resolution transmission electron microscopy (HRTEM) image (Fig. 2g) based on a single nanorod reveals the lattice fringe spacings of 0.312 nm, corresponding to the (310) crystal planes of the tetragonal phase of α-type MnO_2.[23] The selected area electron diffraction (SAED) pattern (Fig. 2h) indicates the poly-crystalline structure of the sample. The SEM and TEM images (Fig. 2b and 2e) show that the as-prepared δ-phased MnO_2 sample exhibits a porous and petal-like structure. The formation of the pores can be attributed to the petal-like MnO_2 sheets randomly stacking together. Fig. 2i shows the HRTEM image of the δ-phased MnO_2 sample. The lattice spacing of 0.245 nm between adjacent lattice planes can be assigned to the (006) facets of δ-phased MnO_2, which is in agreement with 0.244 nm as reported in the literature for δ-type MnO_2.[22] The corresponding SAED pattern, as shown in Fig. 2j, indicates a poly-crystalline nature of the δ-type MnO_2 sample. The morphology of the as-prepared α-phased MnO_2 is shown in Fig. 2c and 2f. It can be seen that the sample mainly consisted of rod-like MnO_2 nanoparticles (Fig. 2c and 2f). Fig. 2k shows the HRTEM image of a single nanorod. The lattice space is measured to be about 0.312 nm, corresponding to the (310) plane of α-MnO_2. The SAED pattern (Fig. 2l) indicates a poly-crystalline structure of the α-MnO_2 sample. Besides the Si signals coming from the silicon substrate, Mn, O, and K were detected from the α+γ-MnO_2, δ-MnO_2 and α-MnO_2 samples in the energy dispersive spectra (EDS), which confirm that most of the graphene reduced $KMnO_4$ to MnO_2 in all the samples (Fig. 2m-2o).

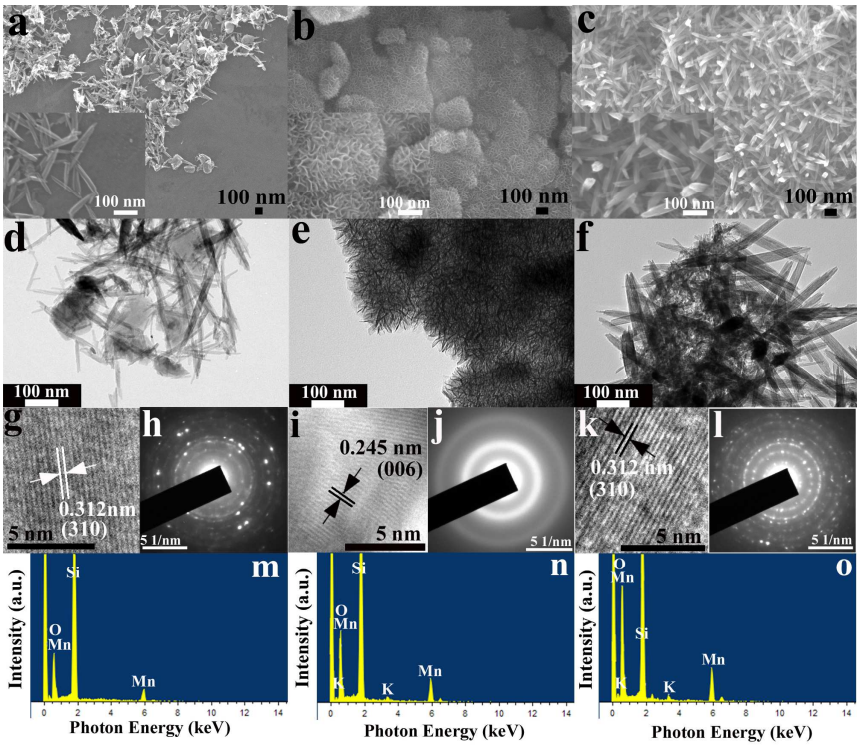

Fig. 2. SEM images of the (a) α+γ-MnO_2, (b) δ-MnO_2 and (c) α-MnO_2 sample. TEM images of the (d) α+γ-MnO_2, (e) δ-MnO_2 and (f) α-MnO_2 sample. HRTEM images of the (g) α+γ-MnO_2, (i) δ-MnO_2 and (k) α-MnO_2 sample. SAED images of the (h) α+γ-MnO_2, (j) δ-MnO_2 and (l) α-MnO_2 sample. A representative EDS spectrum of the (m) α+γ-MnO_2, (n) δ-MnO_2 and (o) α-MnO_2 sample.

The structural change upon redox reaction between graphene and permanganate ions was further characterized by the Raman spectroscopy. Fig. 3a shows the Raman spectra of the graphene, α+γ-, δ- and α-phased MnO_2 samples. The complete disappearance of the D and G bands of the graphene and the appearance of the peaks located at 630 cm^{-1}, which are commonly attributed to the symmetric stretching vibration Mn-O of MnO_6 groups,[14] confirms the formation of MnO_2 and the most of graphene being consumed in the final samples. These results also suggest the

replacement of graphene to MnO_2, instead of forming the graphene-MnO_2 composites.

Figs. 3b-3c show the TGA of the graphene, α+γ-MnO_2, δ-MnO_2 and α-MnO_2 samples in an air atmosphere. The weight loss of 5 - 14 % (5.3 % for α+γ-MnO_2 and α-MnO_2, 14 % for δ-MnO_2 sample) below 200 °C is attributed to the evaporation of the absorbed water in all the samples.[14] A significant weight loss can be observed in the range of 400 - 500 °C for graphene. This feature is associated with the thermal decomposition of the carbon skeleton. Distinctly different from the curves for graphene, only little weight loss in the range of 400 - 500 °C in the curves of α+γ-MnO_2, δ-MnO_2 and α-MnO_2 samples is observed (Fig. 3b-3c). These results imply that most of the carbon has been removed during the direct redox reaction between MnO_4^- and graphene. The weight loss around 545 -650 °C for the α+γ-MnO_2, δ-MnO_2 and α-MnO_2 samples is due to the transformation of MnO_2 into Mn_2O_3 by the evolution of oxygen.[13] These TGA results indicates that most of the graphene has transferred into MnO_2.

The electronic structure of the prepared α+γ-MnO_2, δ-MnO_2 and α-MnO_2 samples were investigated by XPS analysis. Figs. 3d-3l show the representative XPS spectra of the prepared MnO_2 samples. The manganese oxidation state was verified from the multiplet splitting of the Mn 3s peak.[27] This splitting arises from the parallel spin coupling of the 3s electron with the 3d electron during the photoelectron ejection. The energy separation between the two peaks is related to the mean manganese oxidation state.[28] The splitting width is 4.5 eV for α+γ-MnO_2 and α-MnO_2 samples, and 4.8 eV

for δ-MnO_2, which are in accordance with a previous report of MnO_2 (4.78 eV).[28] The peaks of Mn $2p_{1/2}$ and $2p_{3/2}$ which are centered at 653.8 and 642.0 eV for α+γ-MnO_2 and α-MnO_2 samples, and centered at 653.9 and 642.1 eV for δ-MnO_2 samples, respectively, with a spin-energy separation of 11.8 eV,[20] suggesting the formation of MnO_2. Moreover, the peak of O 1s (Fig. S2 in SF) includes a spiking (centered at 529.7 eV for α+γ-MnO_2, 529.6 eV for α-MnO_2 and δ-MnO_2) and a relatively weak peak (centered at 531.9 eV for α+γ-MnO_2, 531.2 eV for δ-MnO_2, and 531.4 eV for α-MnO_2). The two peaks are related to two kinds of oxygen: one is correspond to the [MnO_6] octahedra in the lattice of MnO_2, and the other is the H_2O which is exist between the interlayer of MnO_2 crystal structure.[13] The peaks of the C1s in (d), (g) and (j) result from the carbon conductive tape being used as the substrate.

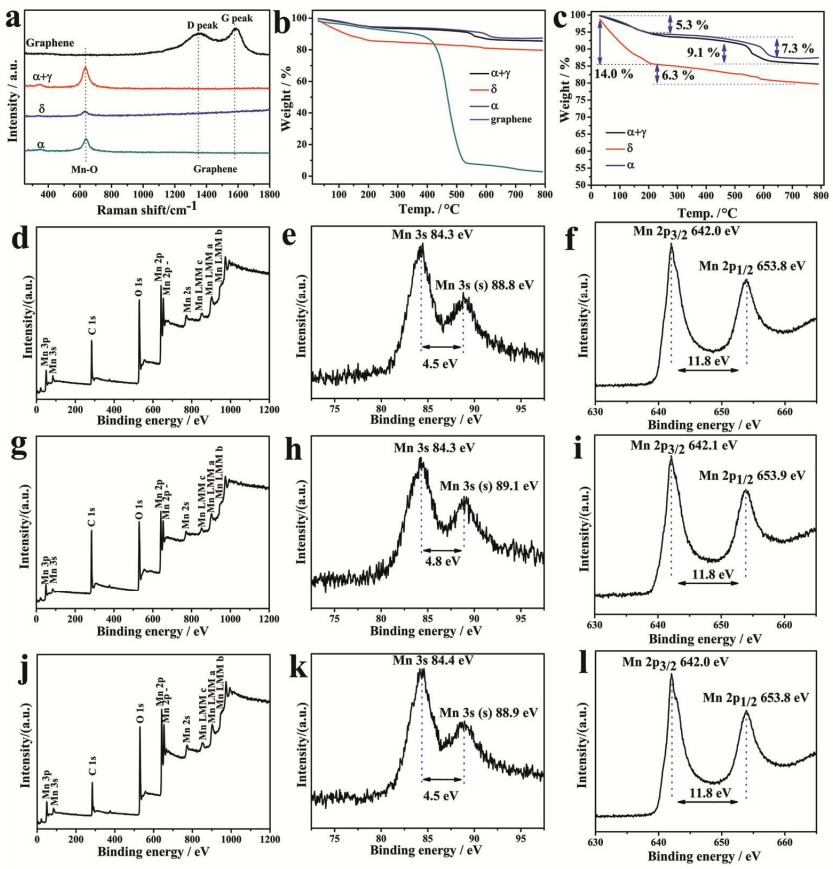

Fig. 3. (a) Raman spectra of the graphene and as-prepared samples. (b) TGA of the graphene, α+γ-MnO_2, δ-MnO_2 and α-MnO_2 samples in an air atmosphere. (c) TGA of the α+γ-MnO_2, δ-MnO_2 and α-MnO_2 samples. XPS spectra of the (d) survey scan, (e) Mn 3s region, and (f) Mn 2p region for the α+γ-MnO_2 sample. XPS spectra of the (g) survey scan, (h) Mn 3s region, and (i) Mn 2p region for the δ-MnO_2 sample. XPS spectra of the (j) survey scan, (k) Mn 3s region, and (l) Mn 2p region for the α-MnO_2 sample.

A typical type-IV isotherm characteristic can be observed for all the MnO_2 samples.[29] The nitrogen adsorption/desorption isotherms show a substantial hysteresis loop in the P/P_0 range above 0.45 for graphene, δ-MnO_2 and α-MnO_2, and 0.8 for α+γ-MnO_2, respectively (Fig. 4). This feature indicates the presence of a lot of

relatively large mesopores in the framework of the obtained MnO_2 samples.[24,29] The pore size distributions for all the samples determined by BJH and HK methods are shown in the inset of Fig. 4. It shows that the α+γ-phased MnO_2 sample consists of micropores (1-2 nm) and a large distribution of mesopores with pore radii between 2 and 50 nm. The δ-phased sample mainly consists of micropores centered at 1 nm and mesopores centered at 3-4 nm. The α-phased sample mainly consists of micropores (1-2 nm) and mesopores (centered at 3-4 nm). The BET surface area of the α+γ-, δ- and α-phased MnO_2 samples were calculated to be 93.7, 140.3 and 84.0 m^2/g, respectively. Remarkably, these values are much higher than the MnO_2 produced by traditional method,[12] indicating the graphene is an ideal template for the synthesis of MnO_2 nanostructures with a high surface area.

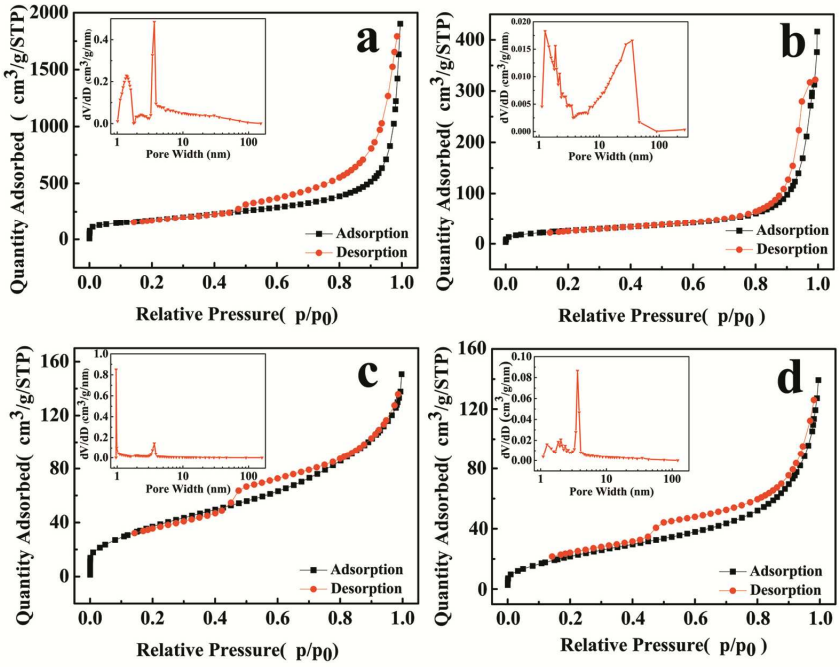

Fig. 4. The nitrogen adsorption–desorption isotherms of (a) graphene, (b) α+γ-MnO_2, (c) δ-MnO_2 and (d) α-MnO_2 samples. The insert shows BJH and H-K pore-size distributions.

To further investigate the role of graphene in the reaction process, the same procedure and recipe were employed as the α+γ-MnO_2 sample but without graphene. As shown in Fig. S1c-A, the solution colour still kept in dark purple after the reaction and no MnO_2 was not obtained, indicating that the reduction of MnO_4^- only in the presence of water was impossible. After the replacement reactions, the solution colour for the α+γ-MnO_2, δ-MnO_2 and α-MnO_2 reaction systems changed from dark purple to black/brown (Fig. S1c in SF), implying the growth of MnO_2 at the cost of the carbon atoms of graphene.

The SEM images and XRD patterns indicate that the amount of H_2SO_4 and the presence of potassium ions have a profound effect on the morphologies and crystallographic structures of the as-prepared MnO_2 nanomaterials. When the mass ratio of graphene to $KMnO_4$ was 1:10 without adding any H_2SO_4, the obtained MnO_2 sample seems to inherit the structure of graphene, which displays a folded and wrinkled sheet-like character with relatively small amounts of flower-like particles decorating on their surface (Fig. 5a and Fig. S3 in SF). The XRD pattern of the sample exhibits the characteristic diffraction peaks corresponding to the pure δ-phased MnO_2 (Fig. 5d, sample $2^{\#}$). When 100 μL or 200 μL H_2SO_4 was added into the above mixture (10 mg graphene and 100 mg $KMnO_4$), the rod-like MnO_2 nanoplarticles with a length around 150 nm and a diameter about 20-30 nm can be observed (Fig. 2c and

Fig. 5b). When the volume of H_2SO_4 was increased from 500 μL to 5 mL, the rod-like MnO_2 structure gradually diminished (Fig. S4 in SF), which should be due to the MnO_2 being corroded by the excessive acid, while the crystalline structure of such samples still display a tetragonal phase of α-type MnO_2 (Fig. 5d, samples $3^{\#}$-$5^{\#}$). When the amount of $KMnO_4$ was increased to 300 mg and the graphene was still maintained at 10 mg with adding 50 μL H_2SO_4, the obtained sample displays the petal-like morphology, as shown in Fig. 5c. The XRD pattern of MnO_2 sample exhibits broad peaks at 2θ = 37.0 and 65.5° with a pure δ-MnO_2 phase (Fig. 5d, sample $1^{\#}$), which is consistent with the above obtained δ-MnO_2 sample (10 mg graphene and 150 mg $KMnO_4$ was used with adding 50 μL H_2SO_4), indicating that the content of potassium ions may be the key factor to form the δ-phased MnO_2.

Based on the above results, the possible formation mechanisms of MnO_2 samples with different morphologies and phase structures are illustrated in Fig. 5e. The reaction process includes two stages, the graphene-driven *in-situ* redox reactionand the ion-driven crystallization.[13] Graphene possesses a lamellar structure with a 2D layer of sp^2-bonded carbon. In the reaction system, carbon atoms of graphene act as a sacrificial reductant when exposed to the $KMnO_4$ solution.[14] The reaction is featured by electron transfer from the carbon to the MnO_4^- ions,[30] and the C–C bonds could be broken and the carbon atoms were fully oxidized to generate CO_2. Simultaneously, elimination the carbon atoms of graphene may lead to the MnO_4^- being reduced and *in situ* forming the [MnO_6] octahedra.[13] The *in situ* transformation from the carbon atoms of graphene to [MnO_6] octahedra of MnO_2 may retain some structure property

of graphene (such as high surface area) to the obtained product. In order to minimize the total energy, the neighboring [MnO_6] octahedra may edge-share for energy stabilization.[13]

However, the question present here is how the [MnO_6] octahedra interlink each other in different way, thus to form various crystal structures (tunnel or layer), when the concentration of the ions (K^+, H^+) are changed. It has been reported that the K^+ cation can favor the formation of different crystallographic structures of MnO_2.[31,32] The $KMnO_4$ in our reaction system can provide K^+, which thus contribute to obtain various crystal structures of MnO_2. We also introduced H_2SO_4 in our reaction system because (i) MnO_4^- are more reactive in the acidic ambient than the H_2SO_4-free system, and hence the graphene is more vulnerable to be oxidated; (ii) the crystallographic structure of the MnO_2 can also be controlled by H^+. It is expected that by using two kinds of crystal oriented cations would crystallize different kinds of MnO_2. We found that the relatively high K^+ concentration and low H^+ concentration facilitates the formation of δ-type MnO_2. Since the spacing in the δ-type MnO_2 is larger than that in the α-type MnO_2, more cations might be required to stabilize their layered structure than the tunneled α-type MnO_2. The experimental results also show that the structural transformation from the layered phase to the tunneled tetragonal phase is strongly dependent on the acidity of the reaction system. With the volume of the H_2SO_4 was further increased, i.e. 100 μL in the reaction solution, the tunnel-structured α-type MnO_2 is formed. It is worth pointing out that the MnO_4^- ions show higher oxidation ability when increase the amount of H_2SO_4, which is necessary to form a more stable

phase of α-MnO_2. In addition, the higher acidity may bring about the contraction of the unit cell, which causes the formation of a more compactness structure that enables it to accommodate the harsh ambient (higher acidity). While the relatively lower concentration of both K^+ and H^+ ions facilitates the formation of a mixed phase of α+γ-MnO_2. It has been proved that the α-phased MnO_2 with the 2 × 2 and 1 × 1 tunnels are more stable than the γ-phased MnO_2, which has a less symmetrical structure of the 1 × 2 tunnel.[33] Therefore, a weaker oxidation ability of MnO_4^- ions resulting from a lower acidity surrounding may induce the formation of the less stable γ-phase MnO_2. In addition, as Sun et al. reported that the lack of K^+ and H^+ can induce the formation of γ-MnO_2.[34] In our experiment, there still exist the low concentration of K^+ and H^+ cations, which thus favors the formation of a mixed phase of α+γ-MnO_2.

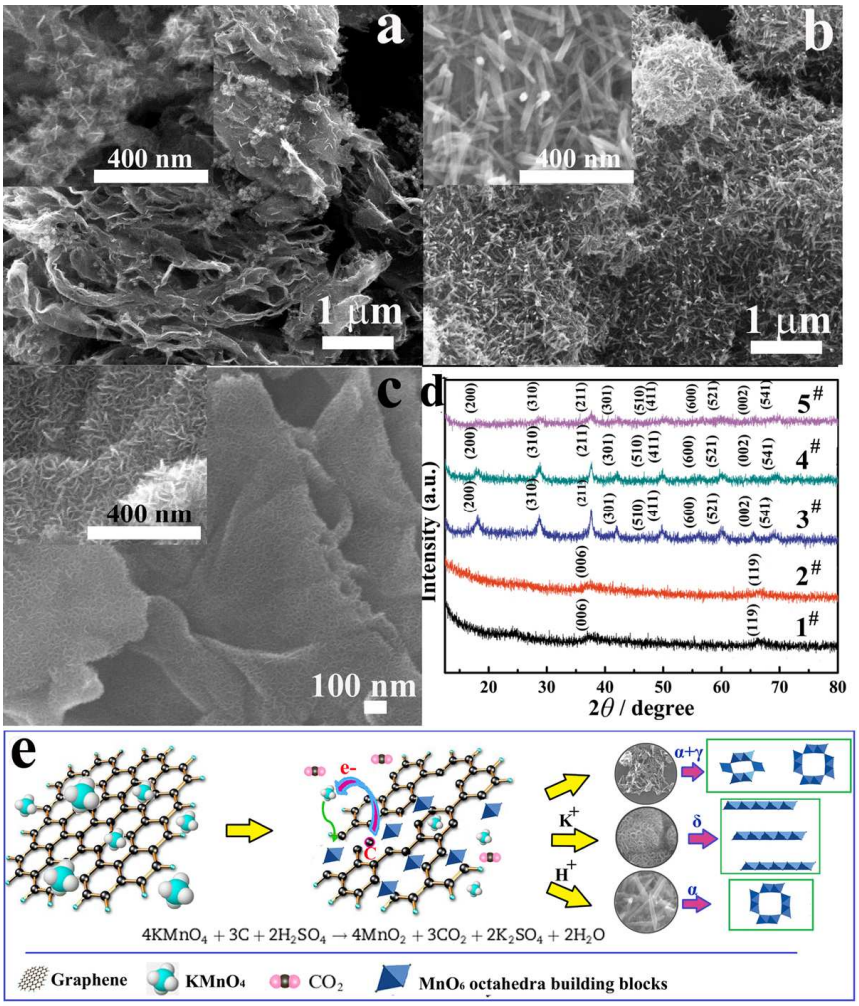

Fig. 5. (a) SEM image of the sample prepared when the mass ratio of graphene : $KMnO_4$ =1 : 10 at 85 °C without adding any H_2SO_4, (b) SEM image of the sample prepared when 10 mg graphene and 100 mg $KMnO_4$ was used at 85 °C with 200 μL H_2SO_4, (c) SEM image of the sample prepared when 10 mg graphene and 300 mg $KMnO_4$ was used at 85 °C with 50 μL H_2SO_4, (d) XRD patterns of the as-prepared samples ($1^{\#}$ was the sample prepared when 10 mg graphene and 300 mg $KMnO_4$ was used at 85 °C with 50 μL H_2SO_4. $2^{\#}$ was the sample prepared when 10 mg graphene and 100 mg $KMnO_4$ was used at 85 °C without adding any H_2SO_4. $3^{\#}$ was the sample prepared when 10 mg graphene and 100 mg $KMnO_4$ was used at 85 °C with 200 μL

H_2SO_4, 4# was the sample prepared when 10 mg graphene and 100 mg $KMnO_4$ was used at 85 °C with 500 μL H_2SO_4, 5# was the sample prepared when 10 mg graphene and 100 mg $KMnO_4$ was used at 85 °C with 5 mL H_2SO_4). (e) Schematic illustration of the formation process for varies of MnO_2 materials with different crystal structures prepared from graphene.

MnO_2, as one of important functional materials, has been widely researched and applied in the field of energy storage, especially in SC. The total charge storage capacity of MnO_2 electrode is dependent on two concurrent parts: (i) the non-Faradic capacitance (i.e., EDLC) accumulated charges at the surface of MnO_2 electrodes via the material surface adsorption or desorption of cations in the electrolyte; (ii) the Faradic capacitance (i.e., pseudocapacitance) that is generated by the intercalation/deintercalation of cations into the MnO_2 lattice during the electrochemical reduction and oxidation process.[35] The charge storage mechanism of MnO_2 materials can be explained by the following reactions in the aqueous electrolytes:[36]

(1) nonfaradic:

$$(MnO_2)_{surface} + C^+ + e^- \rightarrow (MnO_2C^+)_{surface}, (C = H^+, Na^+) \quad (2)$$

(2) faradic:

$$MnO_2 + C^+ + e^- \rightarrow MnOOC, (C = H^+, Na^+) \quad (3)$$

In general, the main part of the capacitance for MnO_2 materials comes from the pseudocapacitive redox process, which strongly depends on their crystallographic structures. The electrochemical properties of the as-prepared α+γ-, δ- and α-MnO_2 samples toward supercapacitor electrode materials were tested under the same conditions. As shown in the cyclic voltammetry (CV) curves in Fig. 6a, symmetric and rectangular CV curves without obvious redox peaks are observed for all the three electrodes, suggesting the fast reversible Faradic reaction and ideal capacitive behavior. The area under the CV curve for δ-MnO_2 electrode is larger than that of α+γ- and α-MnO_2 electrode, suggesting that δ-MnO_2 electrode has the highest specific capacity values among the three samples, and this may due to the large interlayer spacing of the δ-type MnO_2.

The capacitive performance was further investigated by the galvanostatic charge/discharge experiments (Fig. 6b). According to the galvanostatic discharge curves, the corresponding specific capacitances of the samples can be calculated using the following expression: $C_{sc} = (I\Delta t)/(m\Delta V)$, where I is the discharge current, Δt is the total discharge time, m is the mass of active material, ΔV is the potential drop during discharging process and C_{sc} is the specific capacitance.[4,11,37] From the slope of the galvanostatic charge/discharge curves, the total specific capacitance of α+γ-MnO_2, δ-MnO_2 and α-MnO_2 electrodes are calculated to be 60, 160 and 75 F/g, respectively. These specific capacitance values are higher than the previously reported values of 32.8 F/g for α-MnO_2, 24 F/g for γ-MnO_2 prepared by the microwave−hydrothermal method.[32] In order to accurately reflect the energy storage behaviors and

crystallization-dependent electrochemical reaction of the prepared MnO_2 materials, the pure double layer capacitance (based on the specific surface area of the prepared MnO_2 materials) was calculated by using the BET surface area and the average value of 21 μF/cm^2 and give the pure double layer specific capacitance of 19.8, 29.5 and 17.6 F/g for α+γ-MnO_2, δ-MnO_2 and α-MnO_2,[38] which are far lower than the measured value from the galvanostatic charge/discharge measurement, indicating that the main part of the capacitance for MnO_2 materials comes from the pseudocapacitive redox process. Because the pseudocapacitance properties are related to the intercalation/deintercalation of cations into the MnO_2 electrode lattice, thus only the crystallographic structures, which possess a large tunnel size to accommodate these ions, can make a contribution to the capacitance.[1,22] Therefore, the electrochemical property of MnO_2 greatly depended on their crystallographic structures with different tunnels or interlayers. Based on the testing data, it is found that the specific capacitance of the as-crystallized MnO_2 supercapacitors have Faradaic reactivity sequence of δ- > α- > α+γ-MnO_2. This means that the larger interlayer size of δ-MnO_2 (an interlayer separation of ~ 7 Å) is more feasible for the intercalation of cations (Na^+ ions in this case), while the narrow tunnels of α- and γ-phased MnO_2 (2×2, 4.6×4.6 Å and 1×2, 2.3×4.6 Å, respectively) did not facilitate the intercalation of Na^+ ions into the material as well as the δ-MnO_2.

Fig. 6c compares the variation of specific capacitance against current density for the α+γ-, δ- and α-MnO_2 electrodes. It can be seen from the Fig. 6c, the δ-MnO_2 electrode shows the highest specific capacity values among the three samples at

different scan rate. To evaluate the long-life stability of α+γ-, δ- and α-MnO_2 material, cycle charge–discharge testing is employed to examine the service life of the α+γ-, δ- and α-MnO_2 electrodes. The cutoff voltage of all the electrodes is controlled from 0 to 0.9 V at a current density of 1 A/g in 1 M Na_2SO_4 electrolyte. The variations of specific capacitance of the obtained MnO_2 electrodes during cycling are illustrated in Fig. 6d. The capacitance of all the three MnO_2 electrodes increases slightly during the cycling process, most likely due to the electrolyte penetrate into the bulk of electrode materials during the initial cycling process. As for the δ-MnO_2, the specific capacitance after 500 cycles is 147 F/g, which is 20 % higher than the initial value and 6 % lower than the maximum value. As for the α+γ-MnO_2 and α-MnO_2, the specific capacitance after 500 cycles are 46.8 F/g and 65.5 F/g, which are 14 % and 3 % higher than the initial values, indicating that the three MnO_2 working electrodes can withstand 500 cycles with a slight increase in the specific capacitance, exhibiting a high electrochemical stability.

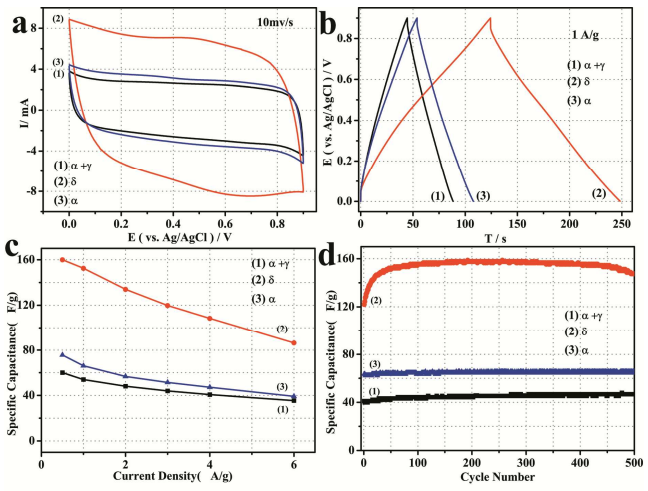

Fig. 6. (a) CV curves of the α+γ-, δ- and α-MnO_2 electrodes at the scan rate of 10 mV/s. (b) Galvanostatic charge-discharge of the α+γ-, δ- and α-MnO_2 electrodes at the

current density of 1.0 A/g. (c) Variation of specific capacitance against current density for the α+γ-, δ- and α-MnO_2 electrodes. (d) Cycling performance of the α+γ-, δ- and α-MnO_2 electrodes.

4. CONCLUSIONS

MnO_2 materials with different crystallographic structures (i.e. α+γ-, δ-, and α-phase) were prepared by using the graphene as a sacrificial template. It was found that higher K^+ cation concentration favors the crystallization of δ-MnO_2, while the α-MnO_2 was produced with higher H^+ cation concentration. Controlable systhesis of optimized crystallographic structures electrode materials are important for the applications of supercapacitors. Electrochemical measurements show that the performance of the as-crystallized MnO_2 supercapacitors is greatly depended on their crystallographic structures. The obtained MnO_2 materials have a Faradaic reactivity sequence of δ- > α- > α+γ-MnO_2. More importantly, the large BET surface areas and controllable crystallographic structures of MnO_2 materials are believed to largely improve its special applications, including catalysis, sensors, adsorbent, etc. We believe that our research may enlarge the potential application of graphene, and provide a possible methodology to product affordable nanomaterials for high-performance supercapacitors.

ACKNOWLEDGEMENTS

We thank Dr. Chuansheng Ma and Dr. Guang Yang from the International Center for Dielectric Research, Xi'an Jiaotong University, for their support with SEM, TEM and

HRTEM. This work is supported by National Natural Science Foundation of China (No. 51271135), the program for New Century Excellent Talents in university (No. NCET-12-0455), the Fundamental Research Funds for the Central Universities, and the project of Innovative Team of Shanxi Province (No. 2013KCT-05).

Supporting Information Available: SEM and TEM images of the pristine graphene. Photographs demonstrating the reaction between graphene and $KMnO_4$ solution. XPS spectra of the O 1s region for the prepared samples. TEM images of the sample prepared when the amount ratio of graphene : $KMnO_4$ =10 mg : 100 mg at 85 ℃ without adding any H_2SO_4. Raman spectra of the graphene and as-prepared samples. SEM image of the sample prepared when 10 mg graphene and 100 mg $KMnO_4$ was used at 85 °C with 500 μL H_2SO_4 and 5 mL H_2SO_4.

REFERENCES

(1) Zhang, Y.; Sun, C.; Lu, P.; Li, K.; Song, S.; Xue, D. Crystallization Design of MnO_2 towards Better Supercapacitance. *CrystEngComm* **2012**, *14*, 5892-5897.

(2) Wei, W.; Cui, X.; Chen, W.; Ivey, D. G. Manganese Oxide-Based Materials as Electrochemical Supercapacitor Electrodes. *Chem. Soc. Rev.* **2011**, *40*, 1697-1721.

(3) Wang, G.; Zhang, L.; Zhang, J. A Review of Electrode Materials for Electrochemical Supercapacitors. *Chem. Soc. Rev.* **2012**, *41,* 797-828.

(4) Mao, L.; Zhang, K.; On Chan, H. S.; Wu, J. Nanostructured MnO_2/Graphene Composites for Supercapacitor Electrodes: the Effect of Morphology, Crystallinity and Composition. *J. Mater. Chem.* **2012**, *22*, 1845-1851.

(5) Hou, Y.; Cheng, Y.; Hobson, T.; Liu, J. Design and Synthesis of Hierarchical MnO_2 Nanospheres/Carbon Nanotubes/Conducting Polymer Ternary Composite for High Performance Electrochemical Electrodes. *Nano Lett.* **2010**, *10*, 2727-2733.

(6) Chen, C. Y.; Fan, C. Y.; Lee, M. T.; Chang, J. K. Tightly Connected MnO_2–Graphene with Tunable Energy Density and Power Density for Supercapacitor Applications. *J. Mater. Chem.* **2012**, *22*, 7697-7770.

(7) Bao, L.; Zang, J.; Li, X. Flexible Zn_2SnO_4/MnO_2 Core/Shell Nanocable Carbon Microfiber Hybrid Composites for High-Performance Supercapacitor Electrodes. *Nano Lett.* **2011**, *11*, 1215-1220.

(8) Yang, P.; Xiao, X.; Li, Y.; Ding, Y.; Qiang, P.; Tan, X.; Mai, W.; Lin, Z.; Wu, W.; Li, T.; et al. Hydrogenated ZnO Core Shell Nanocables for Flexible Supercapacitors and Self-Powered Systems. ACS Nano **2013**, *7*, 2617-2626.

(9) Lu, X.; Zhai, T.; Zhang, X.; Shen, Y.; Yuan, L.; Hu, B.; Gong, L.; Chen, Jian.; Gao, Y.; Zhou, J.; et al. WO_{3-x}@Au@MnO_2 Core-Shell Nanowires on Carbon Fabric for High-Performance Flexible Supercapacitors. *Adv. Mater.* **2012**, *24*, 938-944.

(10) Xie, X.; Zhang, C.; Wu, M. B.; Tao, Y.; Lv, W.; Yang, Q. H. Porous MnO_2 for Use in a High Performance Supercapacitor: Replication of a 3D Graphene Network as a Reactive Template. *Chem. Commun.* **2013**, *49*, 11092-11094.

(11) Lei, Z.; Zhang, J.; Zhao, X. S. Ultrathin MnO_2 Nanofibers Grown on Graphitic Carbon Spheres as High-Performance Asymmetric Supercapacitor Electrodes. *J. Mater. Chem.* **2012**, *22*, 153-160.

(12) Xiao, W.; Wang, D.; Lou, X. W. Shape-Controlled Synthesis of MnO_2 Nanostructures with Enhanced Electrocatalytic Activity for Oxygen Reduction. *J. Phys. Chem. C.* **2010**, *114*, 1694-1700.

(13) Zhao, G.; Li, J.; Jiang, L.; Dong, H.; Wang, X.; Hu, W. Synthesizing MnO_2 Nanosheets from Graphene Oxide Templates for High Performance Pseudosupercapacitors. *Chem. Sci.* **2012**, *3*, 433-7.

(14) Lee, S. W.; Bak, S. M.; Lee, C. W.; Jaye, C.; Fischer, D. A.; Kim, B. K.; Yang, X. Q.; Nam, K. W.; Kim, K. B. Structural Changes in Reduced Graphene Oxide upon MnO_2 Deposition by the Redox Reaction between Carbon and Permanganate Ions. *J. Phys. Chem. C.* **2014**, *118*, 2834-2843.

(15) Huang, X.; Qi, X.; Boey, F.; Zhang, H. Graphene-Based Composites. *Chem. Soc. Rev.* **2012**, *41*, 666-686.

(16) Chen, D.; Feng, H.; Li, J. Graphene Oxide: Preparation, Functionalization, and Electrochemical Applications. *Chem. Rev.* **2012**, *112*, 6027-6053.

(17) Mishra, M.; Alwarappan, S.; Joshi, R. K.; Mohanty, T. Chemically Synthesized Graphene for Electrochemical Biosensing. *Journal of Nanoscience and Nanotechnology*. **2013**, *13*, 4040-4044.

(18) Vusa, C. S. R.; Berchmans, S.; Alwarappan, S. Facile and green synthesis of graphene. *RSC Adv.*, **2014**, *4*, 22470-22475.

(19) Alwarappan, S.; Erdem, A.; Liu, C.; Li C. Z. Probing the Electrochemical Properties of Graphene Nanosheets for Biosensing Applications. J. Phys. Chem. C, **2009**, *113*, 8853–8857.

(20) Chen, S.; Zhu, J.; Wang, X. From Graphene to Metal Oxide Nanolamellas: a Phenomenon of Morphology Transmission. *ACS Nano* **2010**, *4*, 6212-6218.

(21) Truong, T. T.; Liu, Y.; Yang, R.; Trahey, L.; Sun, Y. Morphological and Crystalline Evolution of Nanostructured MnO_2 and Its Application in Lithium Air Batteries. *ACS Nano* **2012**, *6*, 8067-8077.

(22) Devaraj, S.; Munichandraiah, N. Effect of Crystallographic Structure of MnO_2 on Its Electrochemical Capacitance Properties. *J. Phys. Chem. C.* **2008**, *112*, 4406-4417.

(23) Chen, Y.; Zhang, Y.; Geng, D.; Li, R.; Hong, H.; Chen, J.; Sun, X. One-Pot Synthesis of MnO_2/Graphene/Carbon Nanotube Hybrid by Chemical Method. *Carbon* **2011**, *49*, 4434-4442.

(24) Li, B.; Rong, G.; Xie, Yi.; Huang, L.; Feng, C. Low-Temperature Synthesis of α-MnO_2 Hollow Urchins and Their Application in Rechargeable Li^+ Batteries. *Inorg. Chem.* **2006**, *45*, 6404-6410.

(25) Liang, S.; Teng, F.; Bulgan, G.; Zong, R.; Zhu, Y. Effect of Phase Structure of MnO_2 Nanorod Catalyst on the Activity for CO Oxidation. *J. Phys. Chem. C.* **2008**, *112*, 5307-5315.

(26) Benhaddad, L.; Makhloufi, L.; Messaoudi, B.; Rahmouni, K.; Takenouti, H. Reactivity of Nanostructured MnO_2 in Alkaline Medium Studied with a Micro-Cavity Electrode: Effect of Synthesizing Temperature. *ACS Appl. Mater. Interfaces* **2009**, *1*, 424-432.

(27) Lee, J. W.; Hall A. S., Kim, J. D.; Mallouk, T. E. A Facile and Template-Free Hydrothermal Synthesis of Mn_3O_4 Nanorods on Graphene Sheets for Supercapacitor Electrodes with Long Cycle Stability. *Chem. Mater* **2012**, *24*, 1158−1164.

(28) Toupin, M.; Brousse, T.; Belanger, Daniel. Charge Storage Mechanism of MnO_2 Electrode Used in Aqueous Electrochemical Capacitor. *Chem. Mater.* **2004,** *16,* 3184-3190.

(29) Zhou, H.; Liu, L.; Wang, X.; Liang, F.; Bao, S.; Lv, D.; Tang, Y.; Jia D. Multimodal Porous CNT@TiO_2 Nanocables with Superior Performance in Lithium-Ion Batteries. *J. Mater. Chem. A* **2013**, *1*, 8525-8528.

(30) Jin, X.; Zhou, W.; Zhang, S.; Chen, G. Z. Nanoscale Microelectrochemical Cells on Carbon Nanotubes. *Small* **2007**, *3*, 1513-1517.

(31) Dang, T. D.; Banerjee, A. N.; Joo, S. W.; Min, B. K. Effect of Potassium Ions on the Formation of Crystalline Manganese Oxide Nanorods via Acidic Reduction of Potassium Permanganate. *Ind. Eng. Chem. Res.* **2013**, *52*, 14154-14159.

(32) Chen, K.; Noh, Y. D.; Li, K.; Komarneni, S.; Xue, D. Microwave–Hydrothermal Crystallization of Polymorphic MnO_2 for Electrochemical Energy Storage. *J. Phys. Chem. C.* **2013**, *117*, 10770-10779.

(33) Cao, J.; Mao, Q.; Shi, L.; Qian, Y. Fabrication of γ-MnO_2/α-MnO_2 Hollow Core/Shell Structures and Their Application to Water Treatment. *J. Mater. Chem.* **2011**, *21*, 16210-16215.

(34) Sun, M.; Lan, B.; Lin, T.; Cheng, G.; Ye, F.; Yu, L.; Cheng, X.; Zheng, X. Controlled Synthesis of Nanostructured Manganese Oxide: Crystalline Evolution and Catalytic Activities. *CrystEngComm* **2013**, *15*, 7010-7018.

(35) Yeager, M.; Du, W.; Si, R.; Su, D.; Marinković, N.; Teng, X. Highly Efficient $K_{0.15}MnO_2$ Birnessite Nanosheets for Stable Pseudocapacitive Cathodes. *J. Phys. Chem. C.* **2012**, *116*, 20173-20181.

(36) Maiti, S.; Pramanik, A.; Mahanty, S. Interconnected Network of MnO_2 Nanowires with a "Cocoonlike" Morphology: Redox Couple-Mediated Performance Enhancement in Symmetric Aqueous Supercapacitor. *ACS Appl. Mater. Interfaces* **2014**, *6*, 10754-10762.

(37) Jin, M.; Han, G.; Chang, Y.; Zhao, H.; Zhang, H. Flexible Electrodes Based on Polypyrrole/Manganese Dioxide/Polypropylene Fibrous Membrane Composite for Supercapacitor. *Electrochim. Acta* **2011**, *56*, 9838-9845.

(38) El-Kady, M. F.; Strong, V.; Dubin, S.; Kaner, R. B. Laser Scribing of High-Performance and Flexible Graphene-Based Electrochemical Capacitors. *Science* **2012**, *335*, 1326-1330.